Journal of Materials Research and Technology 40 (2026) 1547–1560

Contents lists available at ScienceDirect

Journal of Materials Research and Technology

journal homepage: www.elsevier.com/locate/jmrt

Coupled thermo-mechanical finite simulation of heat treatment effects in wire-arc additively manufactured Inconel 625

Behrouz Bagheri Vanani [a], Gazi Tanvir [b], Mahdi Sadeqi Bajestani [c], Yongho Jeon [d,*], Duck Bong Kim [b,**]

[a] Department of Mechanical Engineering, Tennessee Technological University, Cookeville, TN, 38505, USA
[b] School of Environmental, Civil, Agricultural, and Mechanical Engineering, University of Georgia, Athens, GA, 30602, USA
[c] UHasselt, The Transportation Research Institute (IMOB), Martelarenlaan 42, 3500, Hasselt, Belgium
[d] Department of Mechanical Engineering, Ajou University, Suwan, Gyeongii-do, South Korea

ARTICLE INFO

Keywords:
Inconel 625
Numerical analysis
Phase transition
Thermal history
Residual stress
Multi-material structure
Heat treatment

ABSTRACT

A coupled thermo-mechanical finite element framework was developed to analyze the influence of heat treatment on the thermal history, phase evolution, and mechanical responses of Inconel 625 walls fabricated by wire arc additive manufacturing (WAAM). The model captures transient heat transfer, molten pool behavior, phase transformations, and the resulting residual stress and distortion fields. Mesh sensitivity analysis was performed to ensure numerical stability and computational efficiency. The simulations demonstrate that heat treatment promotes a more homogeneous phase distribution and stabilizes the arc process, resulting in a more uniform residual stress profile. Temperature fields increase nonlinearly with build height, and the stress state transitions from tensile near the substrate to compressive in upper layers. Distortion is more sensitive to heat treatment than residual stress, with notable reductions observed in thin-wall geometries. A multi-material configuration combining stainless steel and Inconel 625 was also modeled, revealing sharp interfacial transitions and characteristic morphological features consistent with experimental observations. Overall, the results provide mechanistic insight into heat-treatment-driven improvements in structural integrity, offering guidance for optimizing WAAM process parameters for both single- and multi-material builds.

1. Introduction

Recently, various nickel-based superalloys have been widely developed due to their notable characteristics, including considerable mechanical strength, resistance to surface degradation, and high-temperature creep resistance [1]. Inconel 625 is one of the applicable nickel-based alloys, including molybdenum and niobium in a nickel-chromium matrix alloy, and has been utilized in various industrial applications, such as aerospace, nuclear reactors, or oil and gas industry components, due to its exceptional physical and mechanical properties in corrosive or elevated temperature environments [2–4]. Generally, nickel-based alloys are known for being difficult-to-cut materials due to their excellent hardness properties, low thermal conductivity, and low elastic modulus [5]. Accordingly, progressive tool wear is an inevitable phenomenon in the machining and manufacturing of nickel-based components. As a result, to minimize material removal and save on costs and input materials, new fabrication methods have been seriously considered for discovery. Additive manufacturing (AM), driven by current economic and industrial demands, has been considered a viable option [6]. AM technology, due to its rapid prototyping advantages, is becoming popular in several construction sectors [7]. Numerous methods of distinct AM techniques are defined, including material jetting, material extrusion, powder bed fusion (PBF), binder jetting, directed energy deposition, selective laser melting (SLM), and sheet lamination [8–11]. Wang and Chou [12] compared the residual stress of Inconel 718 alloys produced by SLM and Electron Beam Melting (EBM). It was shown that components produced by SLM exhibit higher residual stress and cubic texture compared to those produced by EBM, which have lower residual stress and fiber texture. The laser-PBF was used by Zhang et al. [13] to investigate the effect of varying temperature values on the mechanical strength of Inconel 625. They reported that the plasticity of Inconel 625 decreases when the temperature increases to

* Corresponding author.
** Corresponding author.
E-mail addresses: princaps@ajou.ac.kr (Y. Jeon), DBKim@uga.edu (D.B. Kim).

https://doi.org/10.1016/j.jmrt.2025.12.243
Received 27 June 2025; Received in revised form 19 December 2025; Accepted 22 December 2025
Available online 23 December 2025

Table 1
Chemical composition of the Inconel 625 in this study [39,40].

Element	Ni	Cr	Mo	Nb + Ta	Al	Fe	Ti	Si	C	Mn	P	S	Cu	Other
Wt%	64	21.7	8.5	3.8	0.1	0.4	0.17	0.14	0.02	0.1	0.005	0.001	0.01	<0.5

1000 °C, due to a transformation in the fracture mode from transgranular to intergranular. Recently, wire arc additive manufacturing (WAAM), a wire-based directed energy deposition (DED) technology utilizing an electric arc as the heat source and a solid wire as the feedstock material, has garnered significant attention in the construction industry for producing parts with various shapes and geometries [14]. The advantages of WAAM in comparison to other AM methods include low material cost, high deposition rate, and material utilization, as well as a low capital cost of setup and maintenance [15]. Amiri and Naffakh-Moosavy [16] investigated the microstructure and mechanical behavior of stainless steel 316L and Inconel 625 during the WAAM process. They found that a sound interface, without cracks or voids, with higher tensile strength compared to the base materials, is considered a ductile fracture mode for well-bonded joints. The drillability of Inconel 625 produced by WAAM was studied by Ceritbinmez et al. [17]. The results indicated that the higher hardness profile of WAAM specimens yields a higher surface quality in mechanical drilling techniques compared to wrought material.

Inconel 625 has been categorized as a solid solution-strengthened superalloy, and its extraordinary sustainability in critical environments is attributed to the strengthening of its Ni–Cr matrix through the solid solution of Nb and Mo [18]. Although the mechanical behaviors of Inconel 625 are controlled by solid solution strengthening elements, precipitation of secondary phases, namely the δ phase, laves phase, and metal carbides (MC, M_6C, $M_{23}C_6$) fabricated due to melting, remelting, or heat treatment, play a significant effect on mechanical properties of the Inconel 625 favorably [19] or unfavorably [20]. The application of a typical annealing process at 980 °C influences the transforming Laves particles due to recrystallization of the secondary phases [21], but another secondary phase-delta (δ) may be generated due to long-term exposure at elevated temperature value during annealing [22] resulting in a negative effect on ductility [23] and, in some cases, a positive effect on tensile strength [24] and hardness [23]. Consequently, heat treatment would significantly enhance the mechanical properties of Inconel 625 by recrystallizing the secondary phases, thereby addressing various issues, including the stress-relieving influence on built components. A step-by-step recrystallization process with time-temperature dependence is recommended to be applied [25]. Sharma et al. [26] estimated the role of post-heat treatment (PHT) on metallurgical and mechanical behaviors of WAAM-ed Inconel 625. It was concluded that PHT has a constructive influence on microstructure evolution, mechanical characteristics, and corrosion behavior of WAAM-ed Inconel 625. Different heat treatment temperatures were used by Karabulut et al. [27] to analyze the microstructure and wear behaviors of Inconel produced by the AM process. The results indicated that heat treatment above 980 °C influences the microstructure of the AM Inconel alloy and improves its mechanical and wear behaviors. The standard heat treatment procedure, as described by Gallmeyer et al. [28], was employed to analyze the microstructural evolution, specifically dislocation density and phase formation, in laser-PBF additive manufacturing of Inconel. It was reported that the cooling rate can influence the nucleation of γ″ and γ′ precipitates, and desired nanoprecipitate structures can be formed after aging at 720 °C.

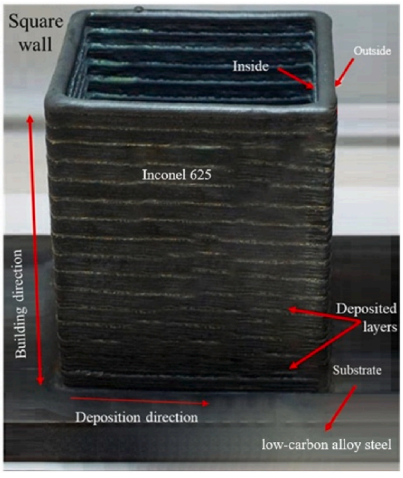

Fig. 1. Square wall of Inconel 625 fabricated by WAAM [39,40].

However, metal deposits manufactured by arc-based AM experience higher thermal issues due to the severe heat input compared to electron- or laser-based AM, and heat accumulation intensifies as the deposition proceeds. To obtain a component with a good deposited geometry, the arc-based AM process typically requires an adequate thermal history to minimize heat accumulation. The involvement of the finite element method (FEM) has been considered a unique tool regarding to predicting the thermal distribution, melt pool characteristics, the level of residual stress, and distortion within the WAAM parts to make it possible for the optimization of the process before the actual WAAM process to reduce overall cost, time, and raw materials [29]. The proper selection of material characterizations, process parameters, and modeling conditions can significantly impact the outcome when compared to real engineering applications [30]. Manurung et al. [31] investigated the numerical method to study the distortion of stainless steel SS316L alloys during the WAAM process. The results indicated that the maximum distortion occurred near the end-start location because of extensive heat. The In-situ thermal management approach was used by Zheng et al. [32] to analyze the thermal history of plasma arc additively manufactured Inconel 625 alloy. It was concluded that the layer-by-layer reduced heat input and the increased temperature preheating between layers of In-situ thermal management led to a distinct residual stress. The FEM analysis was applied by Pramod et al. [33] to investigate the thermal behaviors and mechanical properties of 347 stainless steel (SS347) alloys during the WAAM process. They found that the re-melting phenomenon occurred between additive deposits and projected an inter-layer metallurgical bonding, and the equivalent residual stresses of deposited layers show a uniform pattern. Recently, much more has been carried out in AM, enabling for creation of parts with spatially changing functional behaviors by a combination of various materials/metals into certain functionally graded materials (FGM) and/or multi-material hybrid nanocomposites [34–36]. FGMs exhibit beneficial functionalities and physical characteristics, such as thermal strength, oxidation resistance, or toughness, which can be achieved by optimizing the local application of various metals. Rodrigues et al. [37] applied Twin-WAAM to produce a 316L stainless steel to Inconel 625 FGM under various deposition strategies. It was concluded that the smooth gradient leads to the generation of secondary phases, e.g., Ni_3Nb and carbides, while there is no evidence of the formation of these case phases with the direct interface strategy. Carrol et al. [38] employed the DED method to fabricate an FGM of 304L-Inconel 625 alloys with 24 layers, serving as the transition area, with a composition variation of 4 vol% steps. The results indicated the formation of large cracks (>200 mm) in approximately 21 wt% Inconel 625 and 79 wt% stainless steel.

Based on the above literature, no investigation has been conducted to simulate the effect of heat treatment time on the thermomechanical characteristics of Inconel 625 fabricated by WAAM. This paper aims to

improve a thermo-metallurgical finite element analysis to estimate the thermal history, molten pool, phase transformation, and mechanical properties associated with the heat treatment time of an additively deposited Inconel 625 by WAAM. Additionally, FEM was utilized to study a multi-metal structure comprising Inconel 625-316L regions manufactured by WAAM. The results of this research can enhance the consideration of optimal heat treatment conditions regarding the thermal and mechanical behaviors of Inconel 625 during the WAAM process.

2. Materials and methods

2.1. Experimental procedure

In this investigation, a square wall of Inconel 625 was built additively on an Inconel 625 substrate. Table 1 shows the chemical composition of the used Inconel 625 in the current work. Fig. 1 illustrates the experimentally manufactured sample; the Inconel 625 was deposited on a low-carbon alloy steel substrate. The process parameters and their constant values are obtained based on our previous experimental studies, as reported by Tanvir et al. [39,40]. The square walls of the Inconel-625-WAA-ed sample were heat-treated at 980 °C for 1 h and then air-quenched.

2.2. Numerical simulation

Modeling and simulation of WAAM-ed square-wall Inconel 625 were carried out using the SYSWELD software. The single layer across the square wall is approximately 150 mm long, comprising 20 deposition layers. Typically, the melting efficiency of 0.85 was assigned for arc welding of this material [41]; in this work, an efficiency coefficient of 0.9 was applied to achieve a higher energy efficiency.

2.2.1. Transient heat-transfer analysis

To analyze the thermal and metallurgical fields of deposited layers after WAAM, a fully coupled thermo-metallurgical FE estimation has been applied [42]. Fourier's differential formula was used to analyze the thermal fields, and the phase distribution at each temperature was considered during the thermal analysis of WAAM. Considering different temperatures and phase-dependent material characteristics, e.g., specific heat, the thermal conductivity, inertia effect, and latent heat for each phase transformation, the heat equation in 3D is defined as [43]:

$$\frac{\partial T}{\partial t}=\left(\frac{\lambda}{C}\times\rho\right)\left(\frac{\partial^2 T}{\partial x^2}+\frac{\partial^2 T}{\partial y^2}+\frac{\partial^2 T}{\partial z^2}\right)=\alpha\nabla^2 T \tag{1}$$

In the above equation, T is the temperature (K), t is the time (s), k is the heat conductivity coefficient ($W.m^{-1}.K^{-1}$), C is the specific heat ($J.Kg^{-1}K^{-1}$), q is the mass density ($kg.m^{-3}$), x, y, z are the point coordinates (m), and a is to the thermal diffusivity coefficient (m^2s^{-1}).

2.2.2. Heat source definition

The 3D double ellipsoid heat source analysis is typically applied to arc heat source modeling, which involves two volumetric power sources with similar geometrical shapes. These two parts are used to define the leading and trailing areas of the heat source. Eq. (2) represents the semi-ellipsoid mathematically [44]:

$$Q(x,y,z,t)=\left(6\sqrt{3f_{f,r}Q}\,\Big/\,abc\pi\sqrt{\pi}\right)\exp\left(-\frac{3[x+\vartheta(T-t)]^2}{c^2}-\frac{3y^2}{\alpha^2}-\frac{3z^2}{b^2}\right) \tag{2}$$

In the above equation, Q(x,y,z,t) is the heat input (kJm^{-1}), and v is the velocity (ms^{-1}). The notation f is the fraction for the rear or front quadrant of the heat deposited, while the fraction 'f' (substituted with 'f_f' or 'f_r') is related to forward and rear quadrants, respectively, where the summation of f_f and f_r is ≤ 2. The notation 'a' and 'b' indicate the half-width and the depth of penetration, respectively.

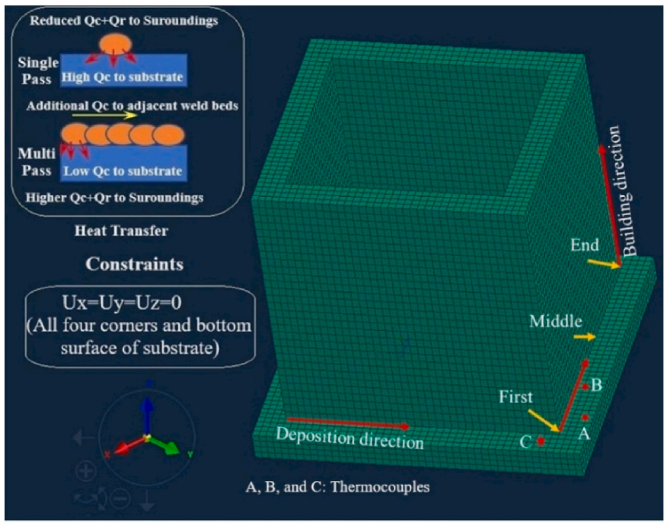

Fig. 2. Mesh, boundary condition, and thermocouple positions in the simulation.

2.2.3. Boundary conditions

Regarding thermal boundary conditions, heat loss results from radiation and convection have been considered a crucial factor in the thermal investigation of a deposition process through WAAM (Fig. 2). The experimental process was carried out at an ambient temperature of 25 °C and Newton's law of cooling and the Stefan-Boltzmann relationship with respect to the convection and radiative losses during WAAM are assigned as [45]:

$$q_c=h(T_s-T_e) \tag{3}$$

$$q_r=\sigma\varepsilon\left((T-T_z)^4-\left((T_0-T_z)^4\right)\right) \tag{4}$$

In the above equations, q_c and q_r are convective and radiative heat transfer, respectively; T_0 is room temperature, ε is the emissivity constant, σ is the Stefan-Boltzmann constant, and T_Z is the absolute zero on the actual temperature scale. In this research, h_c = 5.7 W/m^2K is implemented for the bead, and the top of the substrate material, h_c = 300 W/m^2K is considered for the bottom of the substrate material, ε = 0.2 W/m^2K^4 is used throughout the sample and deposition.

2.2.4. Transient structural analysis

Eq. (5) illustrates the partial differential equations of motion to analyze the residual stresses and deformations [46]:

$$\nabla\sigma+F_b=\rho\ddot{u} \tag{5}$$

In Eq. (5), ∇ is the divergence operator, F_b is the body force vector, σ is the stress tensor, ρ and ü are density and acceleration, respectively. Eq. (6) expresses the relationship between stress and strains:

$$\{\sigma\}=[D]\{\varepsilon^e\} \tag{6}$$

In Eq. (6), σ is the stress vector; $\{\varepsilon^e\}$ is the elastic strain vector, and $[D]$ is the elasticity matrix. The total strain (ε) is defined based on Eq. (7):

$$\varepsilon=\varepsilon^e+\varepsilon^{th}+\varepsilon^p \tag{7}$$

In the above equation, ε is the total strain vector, ε^e is the elastic strain vector, $\{\varepsilon^p\}$ is the plastic strain vector, and $\{\varepsilon^{th}\}$ is the thermal strain vector. However, the stress–strain relationships regarding isotropic material can be given in Cartesian coordinates [47]:

$$\varepsilon_x = \frac{1}{E}\left[\sigma_x - \mu\left(\sigma_y - \sigma_z\right)\right] + \varepsilon_x^p + \varepsilon'$$

$$\varepsilon_y = \frac{1}{E}\left[\sigma_y - \mu\left(\sigma_z - \sigma_x\right)\right] + \varepsilon_y^p + \varepsilon' \quad (8)$$

$$\varepsilon_z = \frac{1}{E}\left[\sigma_z - \mu\left(\sigma_x - \sigma_y\right)\right] + \varepsilon_z^p + \varepsilon'$$

$$\gamma_{xy} = \frac{\tau_{xy}}{2G} + \gamma_{xy}^p;\ \gamma_{yz} = \frac{\tau_{yz}}{2G} + \gamma_{yz}^p;\ \gamma_{zx} = \frac{\tau_{zx}}{2G} + \gamma_{zx}^p$$

In the above equation, *E*, *G*, and μ are the elastic modulus, shear modulus, and Poisson's ratio, respectively.

Eq. (9) expresses the thermal strain:

$$\varepsilon^{th} = \alpha_e \Delta T = \alpha_e (T - T_0) \quad (9)$$

T_0, in Eq. (9), relates to the reference temperature, α_e is the temperature-dependent coefficient of thermal expansion:

$$\varepsilon^{th} = \int_{T_0}^{T} \alpha_e(T) dT \quad (10)$$

In the current model, the Von Mises yield criteria were used, and Eq. (11) is used for equivalent stress:

$$\sigma_e = \sqrt{\frac{1}{2}\left[\left(\sigma_{xx} - \sigma_{yy}\right)^2 + \left(\sigma_{yy} - \sigma_{zz}\right)^2 + \left(\sigma_{zz} - \sigma_{xx}\right)^2 + 6\left(\tau_{xy}^2 + \tau_{yz}^2 + \tau_{zx}^2\right)\right]} < \sigma_f\left(\varepsilon_p, T\right) \quad (11)$$

In Eq. (11), σ_{xx}, σ_{yy}, and σ_{zz} are normal stresses in the X, Y, and Z directions, respectively, while τ_{xy}, τ_{yz}, and τ_{zx} are the shear stresses, σ_f is the flow stress subjected to the plastic strain and the temperature. During the modeling of WAAM, the flow stress plays a significant role in influencing the mechanical behavior of the sample, particularly in terms of residual stress and distortions of the deposited specimen. The SYSWELD software analyzes the net mechanical characteristics of a material as a weighted fraction of the behaviors of each phase. Accordingly, the net yield stress, modulus, and flow curve of Ni-based superalloy, at a distinct instant of time '*t*' and temperature '*T*', is given as [48]:

$$\sigma_{YS}^{net} = f^{\gamma}\sigma_{YS}^{\gamma} + f^{fine\ \gamma'}\sigma_{YS}^{fine\ \gamma'} + f^{coarse\ \gamma'}\sigma_{YS}^{coarse\ \gamma'} \quad (12)$$

$$\sigma_{E}^{net} = f^{\gamma}\sigma_{E}^{\gamma} + f^{fine\ \gamma'}\sigma_{E}^{fine\ \gamma'} + f^{coarse\ \gamma'}\sigma_{E}^{coarse\ \gamma'} \quad (13)$$

$$\sigma_{flow-stress}^{net} = f^{\gamma}\sigma_{flow-stress}^{\gamma} + f^{fine\ \gamma'}\sigma_{flow-stress}^{fine\ \gamma'} + f^{coarse\ \gamma'}\sigma_{flow-stress}^{coarse\ \gamma'} \quad (14)$$

Where, f^{γ}, $f^{fine\ \gamma'}$, $f^{coarse\ \gamma'}$ indicate the phase fractions of the respective phase in the superscript at the distinct point of time, such that $f^{\gamma}+f^{fine\ \gamma'}+f^{coarse\ \gamma'} = 1$.

2.2.5. Phase transformation model

The accuracy of thermal and mechanical analysis in SYSWELD software is dependent on knowledge of the correct mechanical properties during the manufacturing process. The Leblond model and the Johnson-Mehl-Avrami-Kolmogorov (JMAK) model have been applied to analyze the diffusion transformation between various phases. The JMAK model was adopted to study variations in microstructure patterns during thermomechanical processes [49–51]. The JMAK model calculates the growth of second-phase particles with no determination of impingement of the growing particles, and the matrix fraction transformed is presented by:

$$f = 1 - \exp\left(-\frac{\pi}{3}N\vartheta^3 t^4\right) \quad (15)$$

Table 2
Modified SYSWELD phase transformation scheme for Ni-based superalloys [48].

Phase number	Default phases (for steels)	New phase scheme (Ni-base alloy)
Phase 1	Base Material/Ferrite	Coarse γ′
Phase 2	Weld Material	Weld Material
Phase 3	Martensite	Fine γ′
Phase 4	Bainite	Unused Phase
Phase 5	Tempered Martensite	Unused Phase
Phase 6	Austenite	γ

Where, N is the nucleation rate, v and t are the growth rate and the time, respectively. Eq. (16) presents the JMAK model:

$$p = p^{eq}(1 - \exp\left(-t/\tau\right)^n) \quad (16)$$

Or in differential form:

$$\frac{dp}{dt} = n.\left(\frac{p^{eq} - p}{\tau}\right).\left(\ln\left(\frac{p^{eq}}{p^{eq} - p}\right)\right)^{\frac{(n-1)}{n}} \quad (17)$$

Based on the austenite to ferrite/bainite transformations in steel, Eq. (18) was presented by LeBlond [52]:

$$\frac{dp}{dr} = \frac{p_e - p}{\tau} \quad (18)$$

Where p is the current phase fraction, p_e is the equilibrium phase fraction, τ is a time constant calibrated to the rate of the equation. The phase transformation on integrating this equation is presented as the following kinetic equation:

$$\frac{dp}{dt} = 1 - \exp\left(-\frac{t}{\tau}\right) \quad (19)$$

The JMAK equation with a time exponent equal to 1.

Regarding a transformation between two phases A and B, Eqs. (20) and (21) are given as:

$$\dot{p}_A = -k(T)_{p_A} + l(T)_{p_B} \quad (20)$$

$$\dot{p}_B = -k(T)_{p_A} + l(T)_{p_B} \quad (21)$$

In the above equations,

$$k(T) = \frac{p^{eq}}{\tau(T)} \quad (22)$$

$$l(T) = \frac{(1 - p^{eq})}{\tau(T)} \quad (23)$$

LeBlond and Devaux [52] introduced a new model of dependency on the rate of temperature variation by applying a function $h(T)$ associated with the heating or cooling rate:

$$\dot{p}_A = -k(T)h(\dot{T})_{p_A} + l(T)h(\dot{T})_{p_B} \quad (24)$$

$$\dot{p}_B = -k(T)h(\dot{T})_{p_A} + l(T)h(\dot{T})_{p_B} \quad (25)$$

In SYSWELD software, this theory would be presented by identification of the required parameters from the set of the equilibrium phase fraction (PEQ), time constant τ for the reaction (Tau), the temperature rate dependent function (F), and the functions $k(T)$, $l(T)$, and $h(T)$ which are defined by the K, KP, and F respectively.

The SYSWELD software can analyze the phase transformations of up to six phases during the thermomechanical process. The default steel-oriented phase transformation pattern, adapted by Prabhu [48], was used to illustrate the phase transformations between the γ and γ' phases in Ni-based superalloys, as summarized in Table 2.

Based on the phase category in Table 2, the phase transformations will be recognized during heating and cooling conditions as [48]:

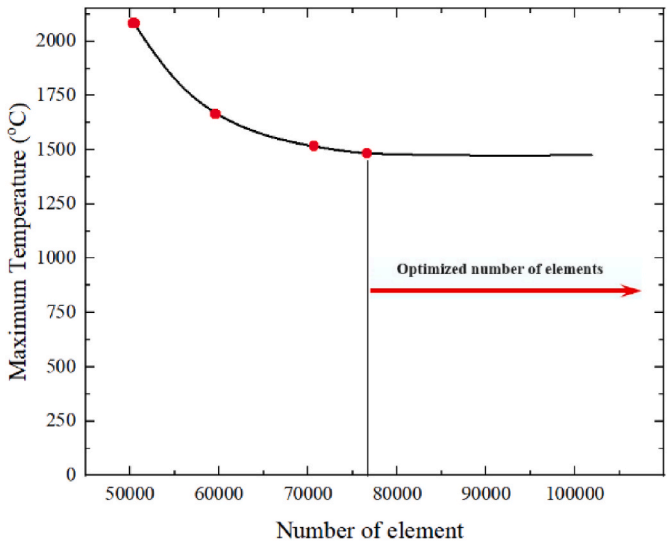

Fig. 3. Mesh sensitivity for maximum temperature as the number of elements increases.

Table 3
Mesh sensitivity and the corresponding maximum temperature and computational time.

Element set	Total number of elements	Computational time (min)	Max temperature (°C)
Set 1	50128	242	2086
Set 2	60020	308	1629
Set 3	71009	376	1511
Set 4	76875	447	1498
Set 5	87638	536	1495
Set 6	99966	624	1497

(1) on heating condition:
- Phase 1 → Phase 6: Coarse γ′ dissolves into γ.
- Phase 2 → Phase 6: Weld material generates γ.
- Phase 3 → Phase 6: Fine γ′ dissolves into γ.

(2) on cooling condition:
- Phase 6 → Phase 3: Fine γ′ precipitates from γ, on cooling.

(3) Both on cooling and on Heating:
- Phase 3 → Phase 1 and Phase 6 → Phase 1: Taken together, these reactions can lead to a passive 'coarsening'.

2.3. Mesh sensitivity analysis

Before applying the numerical analysis, a mesh sensitivity calculation was performed to determine a suitable mesh size for achieving high-accuracy results. Another vital purpose of executing the mesh sensitivity step is related to approaching a tradeoff between data reliability and simulation time. This step in FEM simulation has been considered a simple method to control potential singularity points in the mesh and has been popular among researchers to identify the optimal element number, which not only affects the final result but also plays a vital role in saving time [53–55]. Fig. 2 shows the meshed geometry of the model used for the WAAM process after the mesh sensitivity step, which was performed to obtain an optimized mesh size.

In this regard, a comparison of various element numbers was conducted based on the maximum temperature at the same node. The technique involved dividing a finer mesh on each part, with the total number of elements ranging from 50,128 to 99,996. Fig. 3 shows the mesh sensitivity study graph for various element sizes, and Table 3 summarizes the numerical results of mesh sizes for each number of elements and computational time. Based on the results from Fig. 3 and Table 3, the temperature results are affected by the number of elements used during the FEM analysis; however, the maximum temperature value presents a similar pattern after 76875 elements. Therefore, the number of elements, 76875, was chosen as the optimal mesh size because the number of elements after that does not significantly influence the temperature value and only adds more computational time.

3. Results and discussion

3.1. Thermal analysis

The temperature analysis of the substrate has been easily obtained and plays a significant role in investigating the thermal evolution of deposition layers during the WAAM process. Fig. 4(a) presents numerical results of the temperature history based on the three thermocouple positions shown in Fig. 2. As seen, the temperature distribution shows periodic changes in all three distinguished points on the substrate during each layer deposition. In addition, point A shows the lowest temperature values compared to points B and C due to its faraway location from the thin-wall deposited layers.

To estimate the distribution trend of the temperature gradient, Fig. 4 (b) presents the temperature distribution along the building direction during the WAAM process. It can be observed that the temperature distribution increases non-linearly as the number of deposited layers

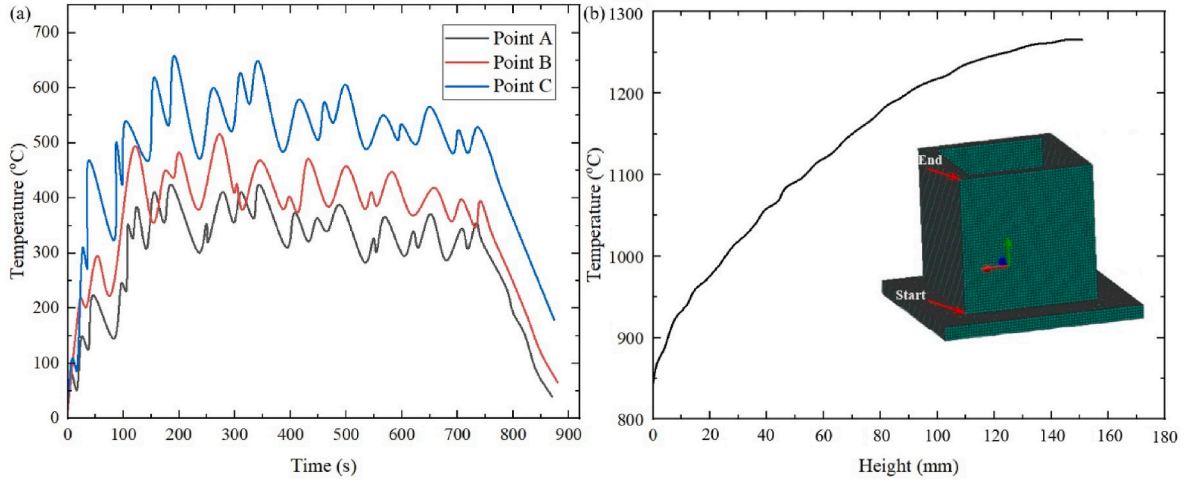

Fig. 4. (a) Comparison of FEM temperature history results on the substrate based on locations defined in Fig. 2 and (b) temperature dispersion along the building direction of deposited layers.

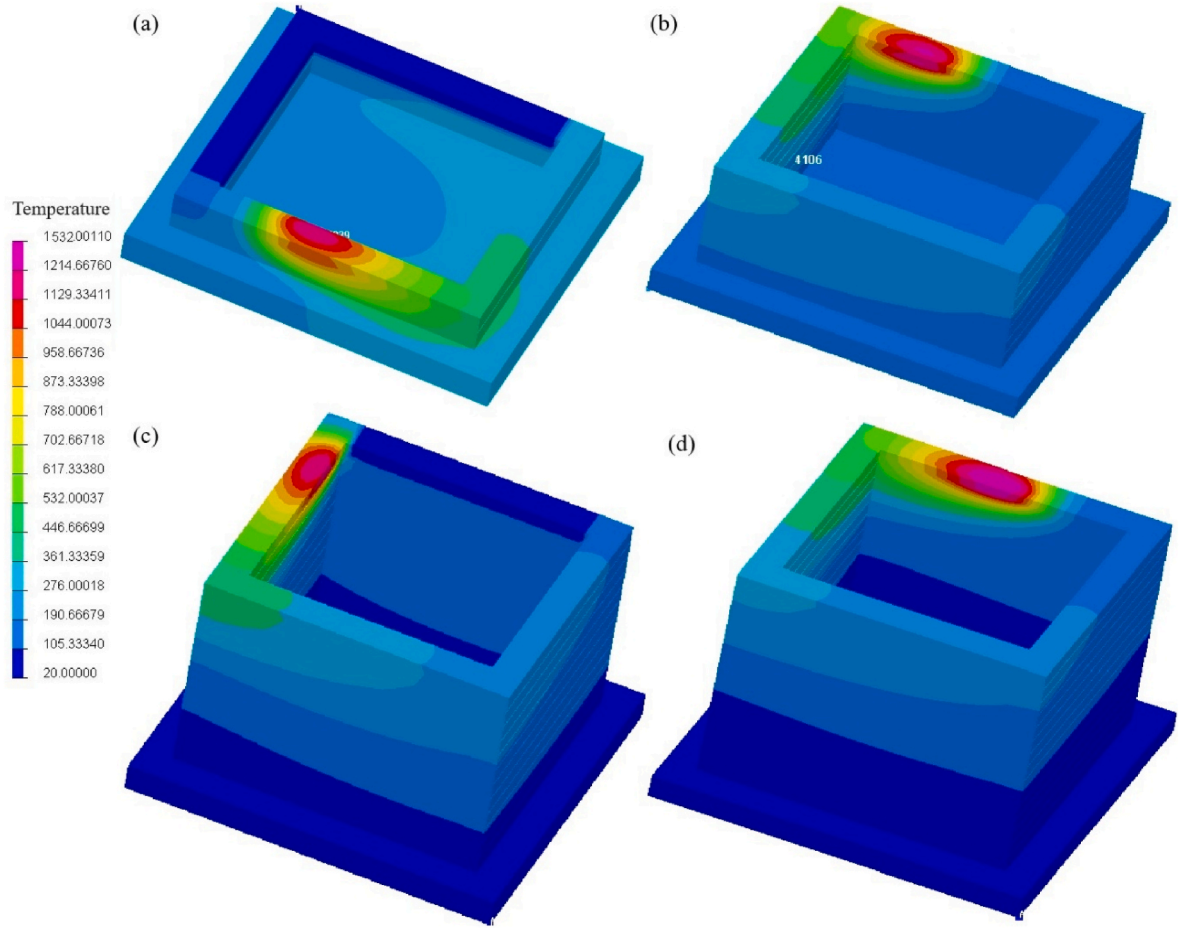

Fig. 5. Temperature contour in various deposited layers from FEM analysis of a square wall of Inconel 625 at (a) 2nd, (b) 9th, (c) 17th, and (d) 20th layer.

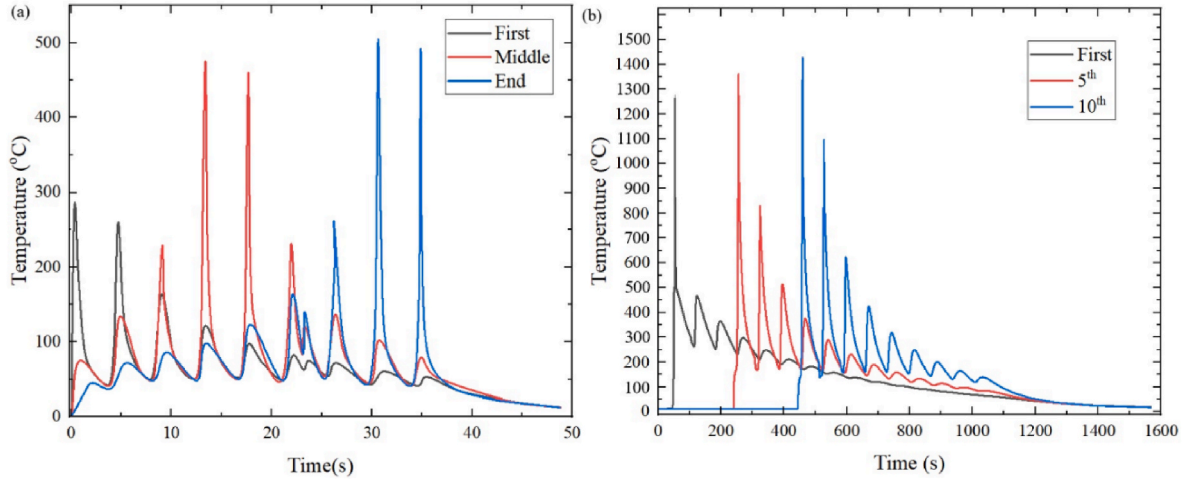

Fig. 6. (a) The thermal cycles of the points "First", "Middle", and "End" (as mentioned in Fig. 2) in the first layer, and (b) the distribution of temperature in the middle point of the deposited wall at various heights of the wall.

increases from the bottom to the upper square-wall model, while the temperature gradient (slope) decreases slowly, indicating a variation in the thermal diffusion conditions along the transfer direction. These outcomes are in good agreement with the reported conclusions by Ding et al. [56]. They indicated a well-distributed volumetric heat source regarding FEM analysis of WAAM on large components.

Fig. 5 presents the evolution of the temperature distribution of multilayer additive depositions when the heat source is at the 2nd, 9th, 17th, and 20th layers. Notably, the deposition of the first layers is associated with faster heating and cooling cycles compared to the upper deposited layers. In addition, thermal gradients at the initial metal deposition are higher due to the ambient temperature [57]. The heat flow to the substrate for the first deposited layers is high, and the heat accumulation in the additive deposits is low. The heat input from the heat source, with an increase in deposited layers and improvement in the deposited wall, becomes greater compared to heat loss, resulting in

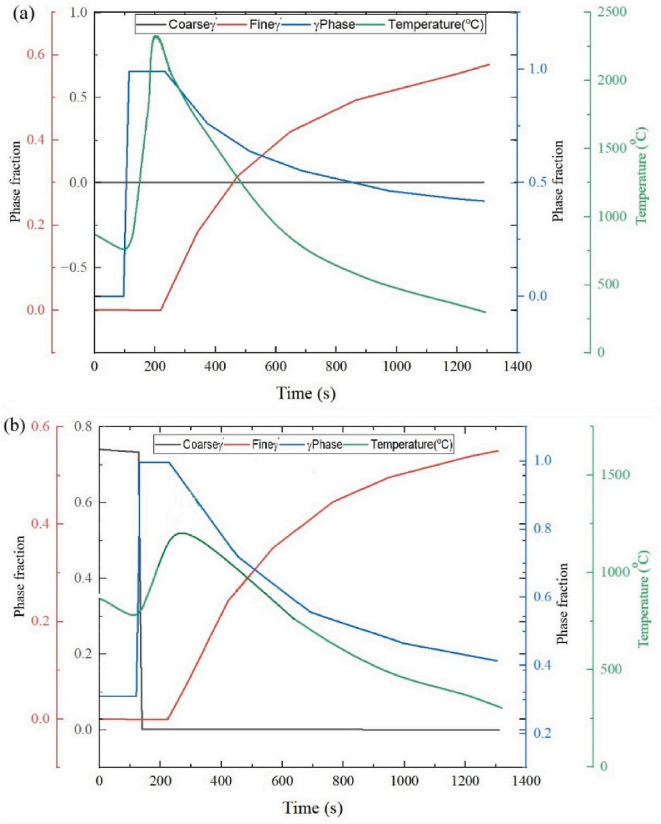

Fig. 7. The evolution of phase fraction and temperature distribution in (a) the melt pool and (b) the HAZ.

thermal accumulation in the additive manufacturing structure [58]. It is observed that the shape and size of the molten pool experience no noticeable variation for different deposited layers, and the melt pool approaches a quasi-stationary state due to the constant input process parameters [59]. Similar results were reported by Chua et al. [60] in their thermo-mechanical analyses of the directed energy deposition process. It was confirmed that the heat was completely transferred to melt the entire width of the activated bead during the multilayer deposition process. The newly activated bead was then melted with a slight overlap with the adjacent bead by introducing a heat source during the planar deposition.

Fig. 6(a) displays the thermal cycles of the points "First", "Middle", and "End" (as mentioned in Fig. 2) in the first layer in a single wall of Inconel 625 obtained by WAAM. As seen, the temperature history of each point has deposition and cooling ranges. Each point, in its own deposition area, experiences different temperature peaks due to an increase in temperature when the arc is started at that point. As the arc moves away and returns, the temperature increases in the second and third stages. However, the first peak temperature for the middle and end points shows a higher value compared to the first point, due to the accumulation of heat from the preheating process. Fig. 6(b) illustrates the distribution of temperature at the middle point of the deposited wall at various heights of the wall. It is evident that the material experiences multiple thermal cycles during the WAAM process, with different falling peak temperatures as the deposition point moves away. As seen, the temperature improves with the development of wall height due to the deposition of upper layers on the resultant bead from the previous layer deposition. The lower layers tend to produce a smaller molten pool because they are surrounded by cold material, whereas the upper layer depositions have a narrower heat conduction channel.

3.2. Phase transformations

Nickel-based alloys include a matrix of FCC γ phase with precipitates of L12 γ' phase and MC metal carbides [61]. In the early stages of nucleation and growth, the γ' phase presents in a near-spherical shape and is considered to have a cubical shape towards the later stages of growth. The alloys, at ambient temperature, include between 65 % and 70 % of γ' phase in the γ matrix. By heating the alloy during the deposition process, the γ' phase dissolves into the matrix and then reprecipitates upon cooling the material. The γ' particles coarsened during long holding periods at high temperature. It has been reported that the mechanical characteristics of alloys are mainly controlled by the evolution of the γ' phase [48,62]. In heating conditions, the LeBlond model, which averages the material, considers the initial state with only coarse γ' and γ phases, indicating that coarse γ' is present for all existing γ' from the beginning of the process. In cooling conditions, the initial reaction is the transformation of the γmatrix to the fine γ' phase.

Fig. 7 displays the obtained LeBlond phase transformation results for a distinct node in the middle layer of a single wall of the sample within

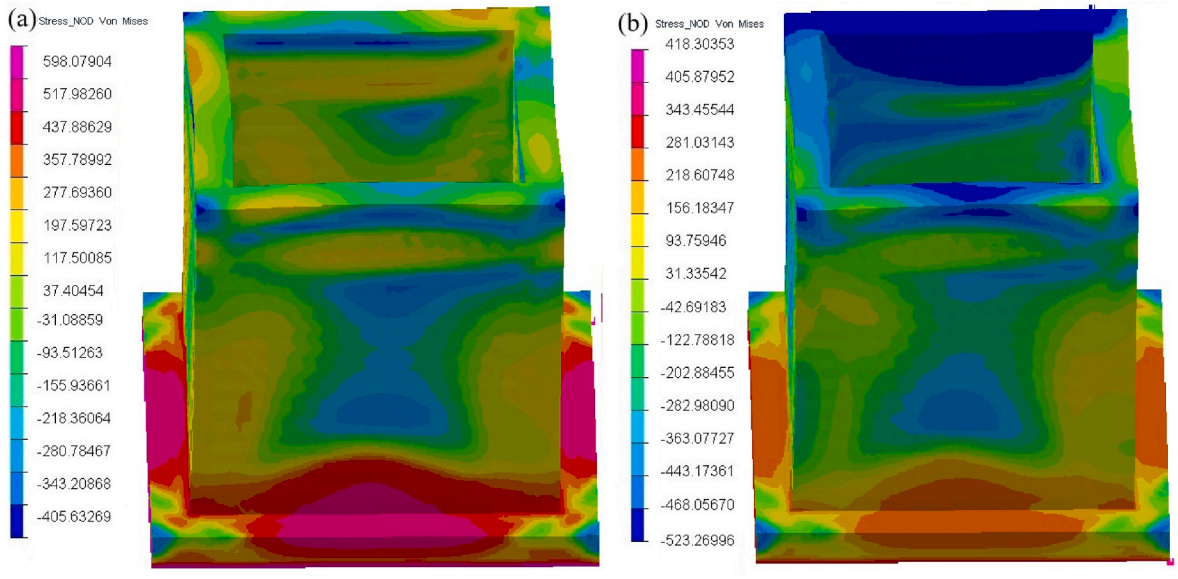

Fig. 8. Residual stress in the square wall of Inconel 625 fabricated by WAAM (a) without heat-treatment and (b) with heat-treatment.

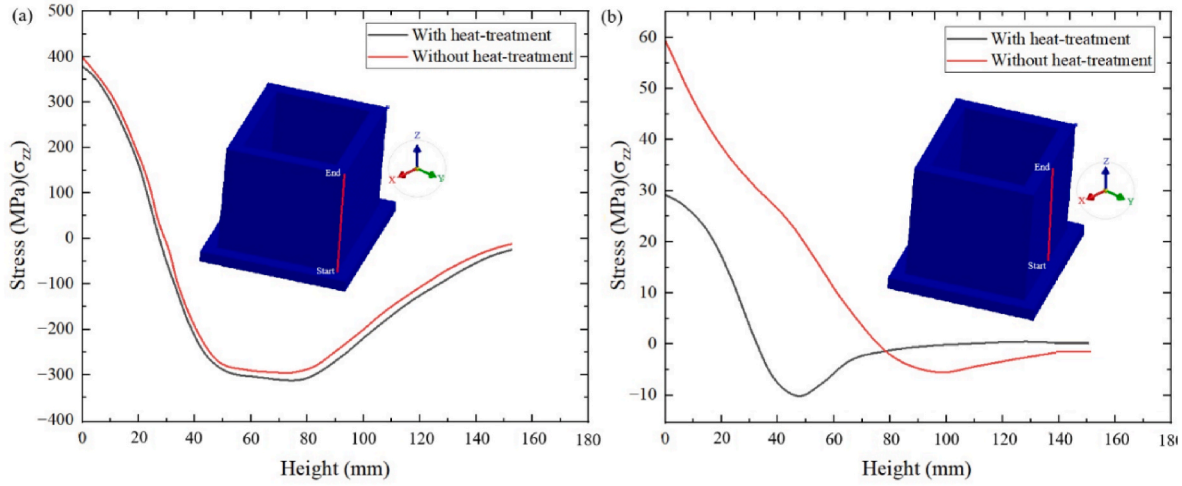

Fig. 9. Normal stress distribution starting from point (a)"First" and point (b)"Middle" along the height.

the molten pool and a node adjacent to the heat-affected zone (HAZ) of the molten pool. Worth noticing is that the fractions of phases range from 0 to 1 in different areas. This is remarkably noticeable from the perspective of studying their effect on mechanical behaviors, especially residual distortions and stresses. Based on the results in Fig. 7(a), the initial phase corresponds to a fictive phase in the molten pool, which transforms to 100 % γ when the deposition layer reaches the specified location. No coarse γ′ was observed in this area, given that this is freshly deposited material. The fine γ′ phase, with a reduction in the temperature values (below the melting point), can be observed to precipitate. Fig. 7(b) indicates that the thermal cycle in the HAZ involves preheating of the workpiece, followed by a temperature increase of approximately 1500 °C, and then cooling. The initial microstructure in this region is compounded by the high amount of coarse γ′ and γ phase. Then, the coarse γ' dissolves with an increase in the temperature values, and the material shows an almost fully γ microstructure at its maximum temperature. This phenomenon is followed by precipitation of the fine phase during the cooling process from the peak temperature.

3.3. Heat treatment effect on residual stress and distortion

The plastic deformation caused by thermal expansion during the deposition process enables the weld bead to experience a compressive stress state. The weld bead, during the cooling process, cannot deform freely due to the applied constraints; hence, it is subjected to tensile forces, and a reduction in temperature results in an increase in these forces. It has been known that clamps or substrates with a large size (especially in depth) are mainly assigned/applied during the WAAM process to ensure fabrication stability. The clamps and substrate, after the WAAM process, will usually be removed by WAAM manufacturers [63]. Fig. 8 presents the total residual stress in the square wall of Inconel 625 produced by the WAAM process with/without heat-treatment. During the WAAM process, the tensile stress from the cooling stage is released through reheating by the additive layer of deposited material, and then compressive stress is produced as the temperature increases until the compressive stress exceeds the compressive yield stress. The compressive stress experiences a reduction in its value as the material undergoes plastic flow. Then, elastic-plastic tensile stress is generated after the material is subjected to the cooling stage [64].

Similar stress evolutions occurred for the material as the heat source traveled to the upper layers. Zheng et al. [32] indicated that the residual stress is much less than the yield stress in most regions of the building direction and the travel direction, while the maximum compressive or tensile residual stress is around or exceeds the YS of Inconel 625 in local regions of the deposits, but much less than the UTS of the deposit. It has been considered that the residual stress in welded or AM-ed compounds can exceed the YS of the material because of the extremely heterogeneous distribution of the temperature field. In addition, the strain

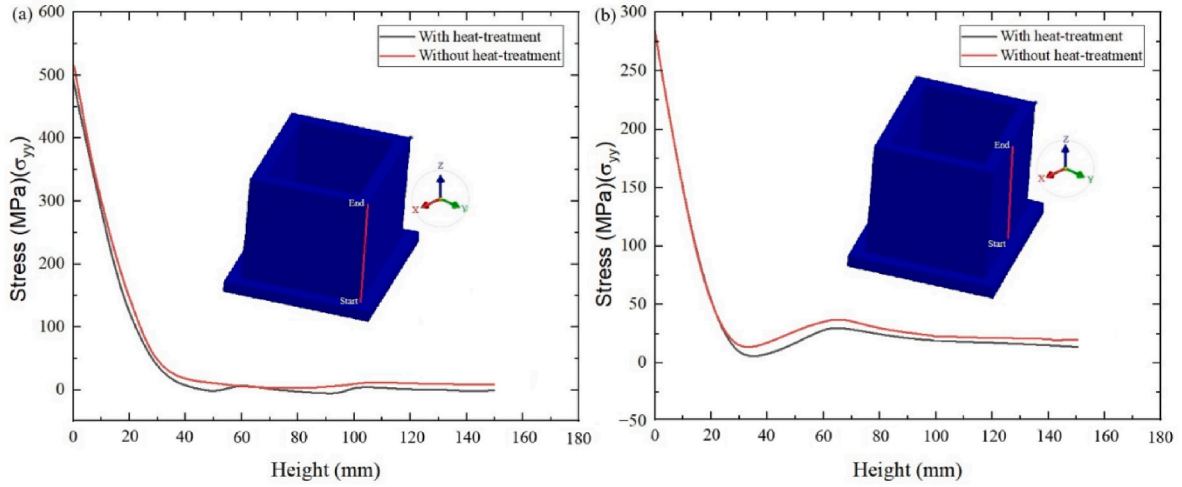

Fig. 10. Traverse stress distribution starting from point (a)"First" and point (b)"Middle" along the height.

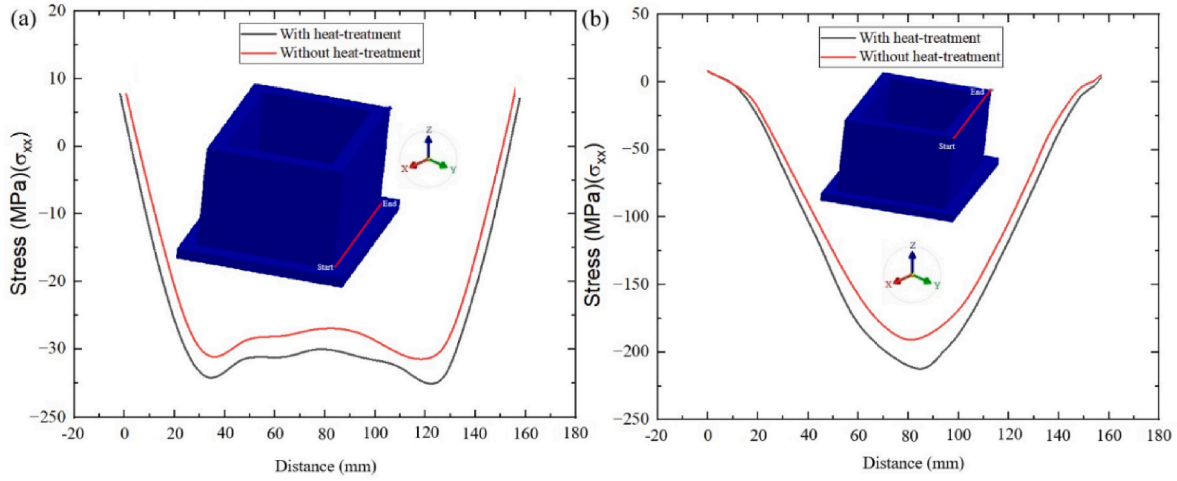

Fig. 11. Longitudinal stress distribution along (a) the bottom and (b) top layers.

hardening resulting from the accumulation of local plastic deformation leads to an increase in the residual stress to exceed even beyond the YS of the material under the unidirectional stress condition.

Figs. 9 and 10 illustrate the normal and traverse stress starting from point "First" and point "Middle" along the height of the wall. In addition, Fig. 11 shows the longitudinal stress distribution along the first and last deposited layers during the process. With an increase in height, the stress decreases and then enters a compressive state. This trend is more pronounced for the first and last deposited layers in Fig. 11, as confirmed by Kohler et al. [65]. They concluded that the bottom surface of the substrate and the first layers of the walls are in tension, while the top layer exhibits high homogeneous compressive residual stress. In addition, the heat treatment leads to a variation in the distribution of stress for higher deposition layers, transitioning from tension to compression due to restrained thermal expansion during reheating, but then increases due to restrained thermal shrinkage. The effect of applied heat treatment on normal stress distribution in the middle part of the wall deposition, as well as longitudinal stress distribution along the first and last deposited layers during WAAM of Inconel 625 alloy, is more pronounced due to higher thermal cycles. The heat treatment has no visible effect on the distribution shape of transverse residual stress in different wall deposition paths, which may be due to a low restriction degree (Fig. 10).

It has been verified that the maximum temperature is a crucial factor in predicting whether or not residual stresses would be affected; that is, the tensile stress with introducing enough peak temperature to the formation of plastic flow will be generated after the material cools down to the ambient temperature, while the elastic stress evolution will be generated in the materials cannot produce residual stresses [66–68]. According to Fig. 11, the plastic deformation caused by thermal expansion during the deposition process results in the weld pool being in a state of compression. During the cooling stage, the weld pool exhibits tensile forces due to the limitation of deformation. The tensile force develops as the temperature decreases. Since an inconsistency exists between the shrinkage deformation of the upper and lower locations of the specimen, the weld bead is compressed, since the substrate is fixed, resulting in compressive stress on the top layer. Shen et al. [69] estimated the effect of in-situ local heat treatment induction heating method on thermomechanical behaviors of manufactured samples

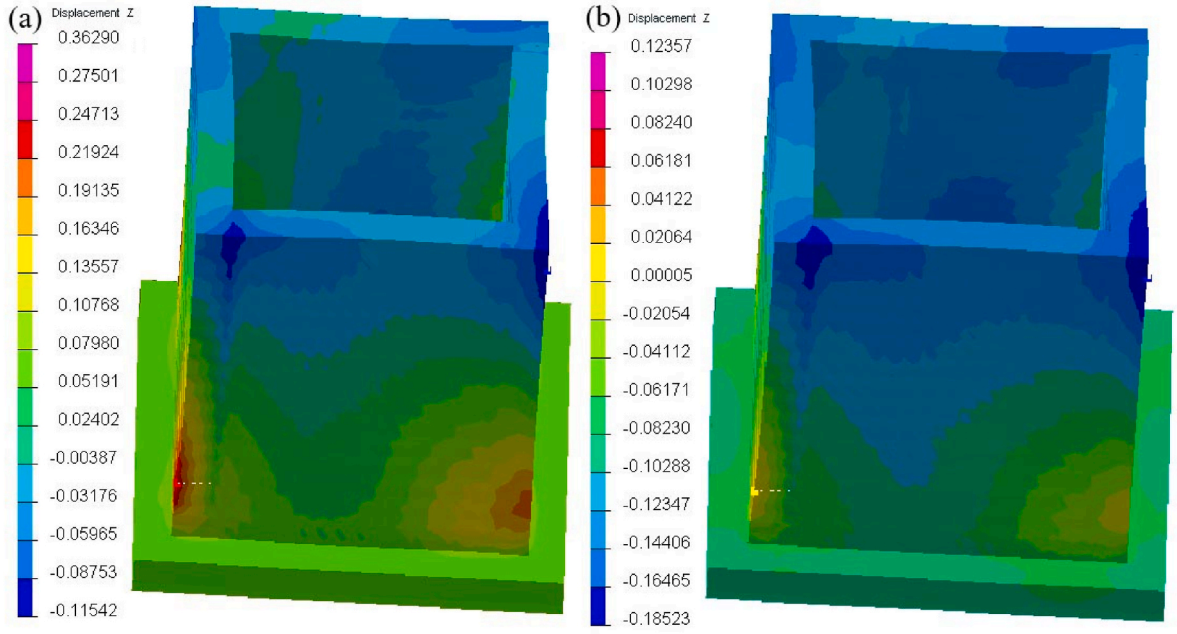

Fig. 12. A contour of normal distortion in the square wall of Inconel 625 fabricated by WAAM (a) before heat treatment and (b) after heat treatment.

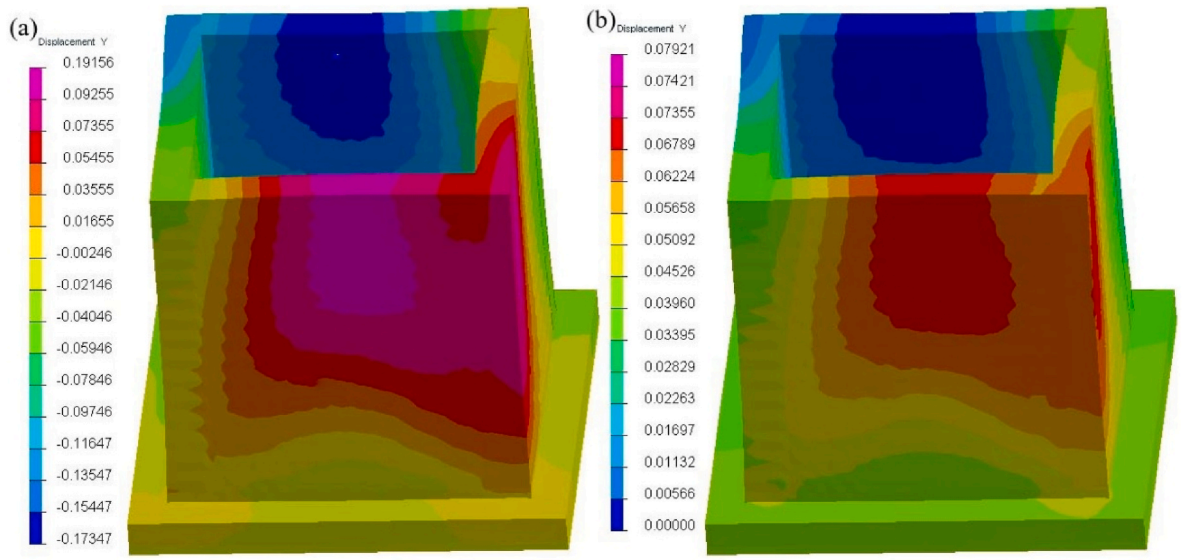

Fig. 13. A contour of traverse stress distribution in a square wall of Inconel 625 fabricated by WAAM (a) before heat treatment and (b) after heat treatment.

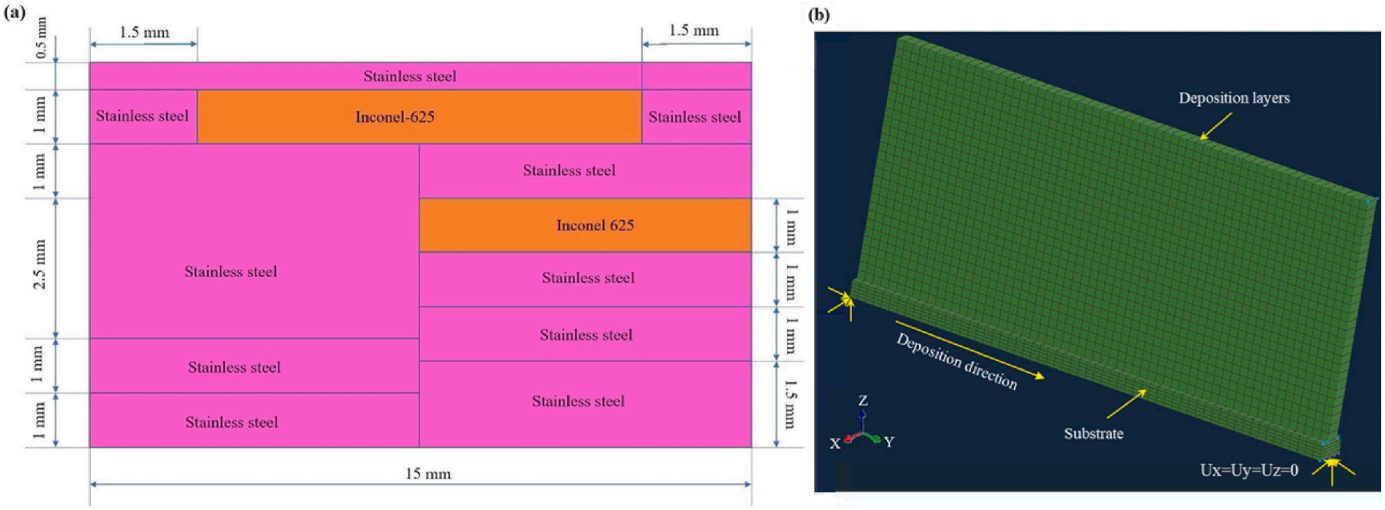

Fig. 14. (a) A schematic (b) FEM modeling of multi-material samples made of Inconel 625 and Stainless steel.

fabricated by WAAM. It was found that an in-situ local heat treatment induction heating method effectively reduced the temperature difference between the heat-treated area and its surroundings. This approach eliminated stress concentration at the corners and improved the uniformity of the stress distribution.

According to Tanvir et al. [39], the inside of the deposited wall exhibits higher mean roughness compared to the outside area due to the difference in cooling rates during the WAAM process. The outside surface rapidly cooled down and developed plastic tensile stress. The inside surface, during solidification, underwent a lower cooling rate than the outside area due to the influence of the high-temperature weld metal nearby, resulting in low convection cooling. The gradual reduction in temperature decreases the temperature gradient of the molten pool during the solidification and cooling periods, playing a beneficial role in reducing residual stress [70,71]. Heat treatment plays a vital role in achieving stable arc characterization and improving process stability through the uniform distribution of residual stress, resulting from the homogenization of phases [68].

It has been known that the metal deposits manufactured by the arc-based AM experience more severe thermal issues because of the high heat input in comparison to other AM techniques, such as laser- or electron-beam-based AM, while the heat accumulation enhances as the deposition proceeds [72]. The successive layer deposition process, with no further attempt to mitigate heat accumulation, will lead to decreased heat dissipation conditions for the molten pool, resulting in a larger molten pool size that grows along the building direction [73]. This, in turn, leads to nonuniform track morphology or noticeable distortions [74]. Therefore, to achieve a sound deposit with good geometry, the arc-based additive manufacturing process typically employs adequate thermal management to minimize heat accumulation. Figs. 12 and 13 present a comparison of normal and traverse distortion in the square wall of Inconel 625 fabricated by WAAM with/without heat treatment conditions. The influence of current heat treatment on the reduction of distortion of wall-thin deposited samples is more significant compared to residual stress.

3.4. The multi-material samples

In the WAAM process, differences in thermophysical properties among various filler materials can lead to stress concentration, increasing the risk of cracking in the parts. Fig. 14 illustrates the schematic and FEM model of multi-material specimens with dimensions of

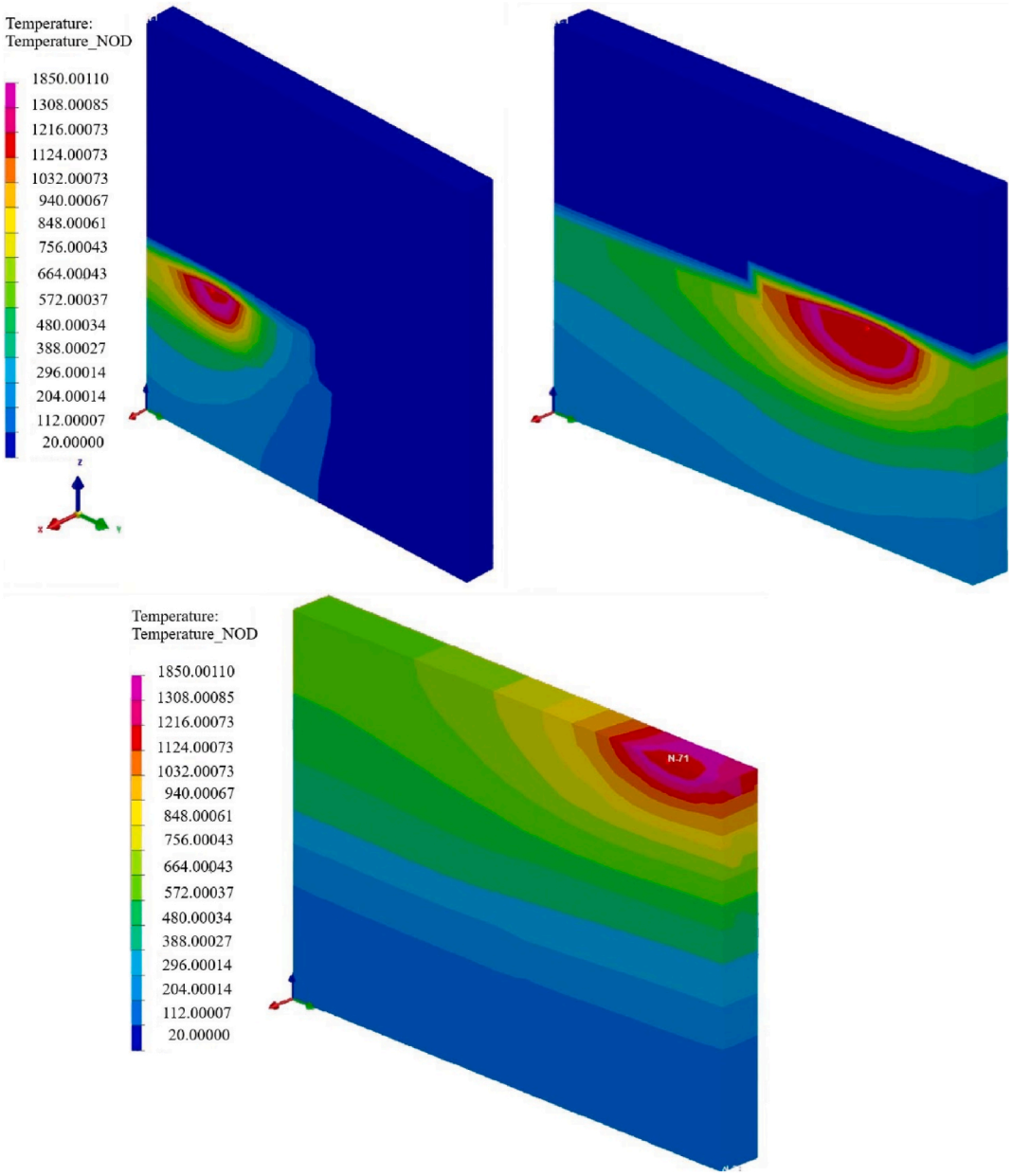

Fig. 15. Temperature contour of deposited layers in the different layers during WAAM.

(15 × 7 × 0.5) mm^3 that were fabricated by wire arc additive manufacturing. In this case, due to the similarity between the lattice parameters of steel S316L and IN625 (3.5948 and 3.5952 Å, respectively), the structure was alternated twelve times along the building direction to analyze the complex structure-property relationship of the manufactured three-dimensional metal specimen at various length scales. The deposition direction is bidirectional and is positioned at the center of the substrate. The total number of nodes in the model is 14650, and the total number of elements is 11895.

The distribution of temperature in different layers of the multi-material structure during the WAAM process is illustrated in Fig. 15. As the number of deposited layers increases, the high-temperature region in the cross-sectional direction gradually expands, and the temperature at the center of the heat source is significantly higher than that of the lower deposited layer. As shown, the thermal dispersion, specifically the melting pool and HAZ, altered continuously in synchrony with the torch movement. Given the spatially symmetric and uniform pattern of the ellipsoid surface of the molten pool, the thermal contours are compressed in front of the torch and expanded behind the molten pool. In the center of the molten pool, the peak temperature far surpassed the melting point, while being lower than the evaporation points of the materials. It increased quickly at first with the deposited layers and continuously reached a stable condition.

As the deposited layer grows, the stress distribution is continuously altered as a result of the geometry change and the accumulation of plastic strain. The FEM cross-section in Fig. 16 illustrates a distinct separation of stainless steel and Inconel phases along the building direction, with morphologically sharp and diffuse interfaces at the material transitions from stainless steel to Inconel and vice versa. The latter interface illustrates phase intermixing with a transition zone resulting from the solvation of the Ni face-centered crystal structure up to approximately 50 wt% of alloying elements [75]. Vertical to the building direction, structural defects can be seen because of a lack of binding here, and the observation of micro-cracks propagating fundamentally along high-angle grain boundaries (HAGBs) in Inconel 625 for the same reason [76].

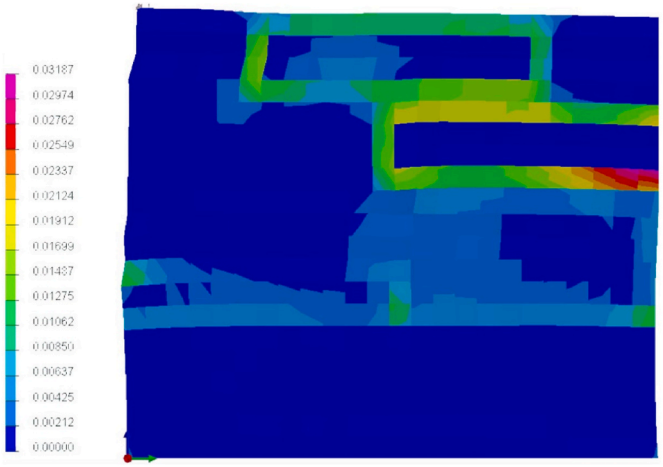

Fig. 16. The FEM cross-section indicates the observation of micro-cracks in Inconel areas of the multi-metal specimen.

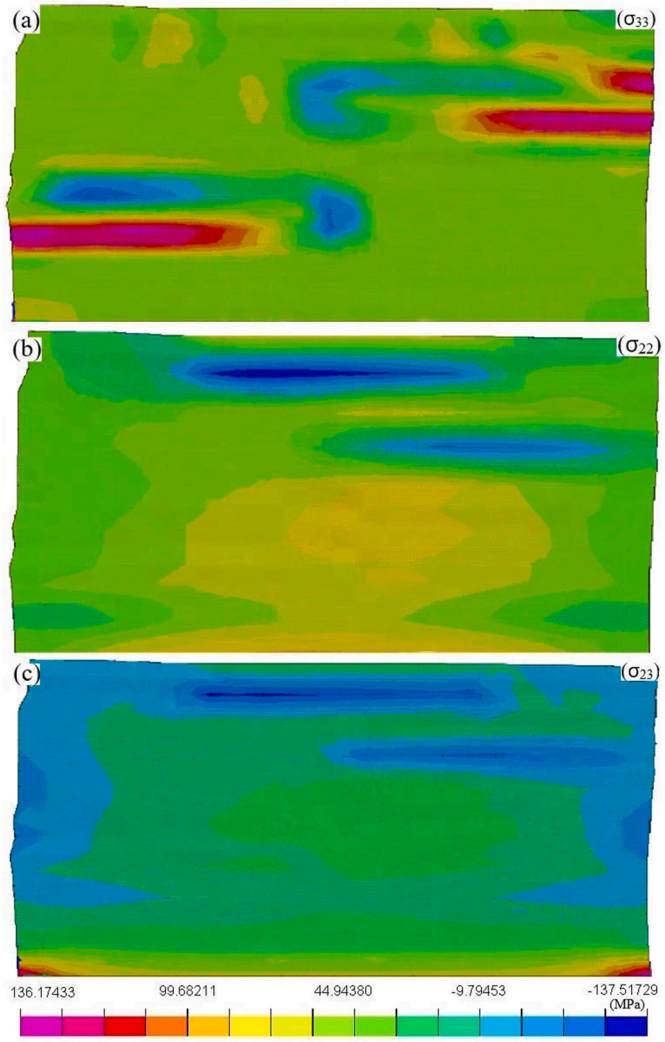

Fig. 17. The FEM distribution of residual strain in the deposited layers for (a) in-plane normal stresses, (b) out-of-plane normal stresses, and (c) shear stresses.

The additive manufacturing process is characterized by rapid heating and cooling, which leads to a large temperature gradient, which is also the main reason for the generation of residual stress [77]. During the deposition process, the free boundaries on both sides of the thin-walled part can help alleviate residual stress to some extent. Fig. 17 shows the FEM residual stresses in-plane, out-of-plane, and shear stresses in the multi-material specimens. In-plane residual stresses cause the upper layers to experience solidification cracking and crack propagation parallel to the building direction (along the Z direction). Additionally, the experimental investigation by Bodner et al. [75] revealed that stress concentrations were observed in both phases when transitioning from Inconel 625 to stainless steel. The maximal tensile stresses are detected at the top right of the specimen area due to the superposition of the stress component resulting from the temperature gradient mechanism [78] and the stress component induced during the cool-down phase of the melted upper layers. Abusalma et al. [79] analyzed the WAAM process to deposit Inconel 718 thin-walled parts on A36 steel substrates, studying the effect of interlayer residence time on the distribution of residual stress. The results indicated that shorter interlayer residence times lead to heat accumulation on the wall during deposition, noticeably increasing residual stress. Conversely, with longer interlayer residence times, the temperature distribution became more even, leading to a more consistent stress distribution throughout the component.

4. Conclusion

In this paper, the influence of a heat treatment procedure was modeled using the FEM technique on WAAM IN625 alloys to improve the structural behavior and enhance the mechanical properties of the samples. Additionally, a multi-metal structure comprising stainless steel and Inconel 625 regions was modeled. The mesh sensitivity for various element sizes, considering the number of elements and computational time, was examined. The following conclusion can be drawn:

- Heat treatment plays a vital role in stable arc characterization and better process stability to uniform distribution of residual stress due to the homogenization of phases.
- The thermal analysis from successive deposited layers was related to the phase and residual stress generation and subsequent evolution.
- With an increase in height, the stress decreases and then becomes a compressive state, and the heat treatment leads to a reduction in the distortion of the square wall deposition.
- In a multi-metal structure, a sharp morphological stainless steel to Inconel 625 interface along the specimen's build direction was observed.

Data availability statement

The data will be made available upon request.

Credit author statement

Behrouz Bagheri Vanani: Writing – original draft, Visualization, Validation, Software, Methodology, Investigation, Formal analysis, Data curation, Conceptualization. Gazi Tanvir: Writing – review & editing, Methodology, Conceptualization. Mahdi Sadeqi Bajestani: Writing – review & editing, Methodology, Formal analysis, Data curation. Yongho Jeon: Writing – review & editing, Project administration, Funding acquisition, Data curation, Conceptualization. Duck Bong Kim: Writing – review & editing, Supervision, Resources, Project administration, Methodology, Investigation, Conceptualization.

Declaration of competing interest

The authors declare that they have no known competing financial interests or personal relationships that could have appeared to influence the work reported in this paper.

Acknowledgements

This work was supported by the National Research Foundation of Korea (NRF) grant funded by the Korea government (MSIT) (No. RS-2024-00346883).

References

[1] Thellaputta GR, Chandra PS, Rao CSP. Machinability of nickel-based superalloys: a review. Mater Today Proc 2017;4(2, Part A):3712–21. https://doi.org/10.1016/j.matpr.2017.02.266. ISSN 2214–7853.
[2] Babu A, Ebrahimi A, Wu KH, Richardson IM, Hermans MJM. Local control of microstructure and mechanical properties of high-strength steel in electric arc-based additive manufacturing. J Mater Res Technol 2023;26:1508–26. https://doi.org/10.1016/j.jmrt.2023.07.262.
[3] Mookara R, Seman S, Ren J, Amirthalingam M. Influence of droplet transfer behaviour on the microstructure, mechanical properties and corrosion resistance of wire arc additively manufactured Inconel (IN) 625 components. Weld World 2021. https://doi.org/10.1007/s40194-020-1043-6.
[4] Cheepu MM, Lee C, Cho S-M. Microstructural characteristics of wire arc additive manufacturing with Inconel 625 by super-TIG welding. Trans Indian Inst Met 2020. https://doi.org/10.1007/s12666-020-01915-x.
[5] Jiang Qi, Zhang P, Yu Zhishui, Shi H, Li S, Di Wu, Yan H, Ye X, Chen J. Microstructure and mechanical properties of thick-walled INCONEL 625 alloy manufactured by WAAM with different torch paths. Adv Eng Mater 2020. https://doi.org/10.1002/adem.202000728.
[6] Ahsan MRU, et al. Microstructures and mechanical behavior of the bimetallic additively-manufactured structure (BAMS) of austenitic stainless steel and Inconel 625. J Mater Sci Technol 2021;74:176–88. https://doi.org/10.1016/j.jmst.2020.10.001.
[7] Jadhav Sainand, Bajestani Mahdi Sadeqi, Islam Saiful, Karim Md Abdul, Kim Chang Jon, Lee Ho-Jin, Cho Young Tae, Kim Duck Bong. Materials characterization of Ti6Al4V to NbZr1 bimetallic structure fabricated by wire arc additive manufacturing. Mater Today Commun 2023;36:106934. https://doi.org/10.1016/j.mtcomm.2023.106934.
[8] Ahsan MdRU, Seo Gi-Jeong, Fan Xuesong, Liaw Peter K, amirhossein Motaman Seyed, Haase Christian, Kim Duck Bong. Effects of process parameters on bead shape, microstructure, and mechanical properties in wire + arc additive manufacturing of Al0.1CoCrFeNi high-entropy alloy. J Manuf Process 2021;68:1314–27. https://doi.org/10.1016/j.jmapro.2021.06.047.
[9] Abbasi Mahmoud, Vanani Behrouz Bagheri, Abdollahzadeh Amin, Sadeqi Bajestani Mahdi, Mohammadkhah Melika, Klinge Sandra. CNT-induced microstructural evolution in Al matrix composite made by additive manufacturing and studying the effect of CNT presence on mechanical and tribological properties. Results Eng 2025;27:106782. https://doi.org/10.1016/j.rineng.2025.106782.
[10] Bagheri Vanani Behrouz, Islam Saiful, Bajestani Mahdi Sadeqi, Jeon Yongho, Kim Duck Bong. Microstructure evolution and mechanical behaviors of Ti6Al4V/NbZr1 bimetallic additively manufactured structure: a molecular dynamics simulation. Int J Manag Res Technol 2025;37:3466–77. https://doi.org/10.1016/j.jmrt.2025.07.025.
[11] Bagheri Vanani Behrouz, Abbasi Mahmoud, Amin Abdollahzadeh. A new investigation on graphene-reinforced 304L nanocomposite made by additive manufacturing process: microstructure and tribology study. J Mater Res Technol 2024;32:674–86. https://doi.org/10.1016/j.jmrt.2024.07.137.
[12] Wensrich CM, Luzin V, Hendriks JN, Pant P, Gregg AWT. Residual stress in additively manufactured Inconel cubes; Selective Laser Melting versus Electron Beam Melting and a comparison of modelling techniques. Mater Des 2024;244:113108. https://doi.org/10.1016/j.matdes.2024.113108.
[13] Zhang Hui, Zhang Daohua, Zhu Iiulong, Ding Molei, An Xudong, Wu Daijiang, Feng Man, Sha Gang, Hu Wangyu, Yang Tengfei. High temperature embrittlement of Inconel 625 alloy manufactured by laser powder bed fusion. Materials Sience and Technology A 2024;900:146506. https://doi.org/10.1016/j.msea.2024.146506.
[14] Islam Saiful, Seo Gi-Jeong, Ahsan MdRU, Villarraga-Gómez Herminso, Lee Ho-Jin, Kim Duck Bong. Investigation of microstructures, defects, and mechanical properties of titanium-zirconium-molybdenum alloy manufactured by wire Arc additive manufacturing. Int J Refract Metals Hard Mater 2023;110:106042. https://doi.org/10.1016/j.ijrmhm.2022.106042.
[15] Islam S, Ahsan MR, Seo G, Lee H, Park T, Pourboghrat F, Kim DB. Investigations of microstructure and mechanical properties in wire arc additively manufactured niobium-zirconium alloy. Adv Eng Mater 2023. https://doi.org/10.1002/adem.202201633.
[16] Amiri Vahid, Naffakh-Moosavy Homam. Wire arc additive manufacturing of functionally graded carbon steel-stainless steel 316L- Inconel 625: microstructural characterization and mechanical behavior. Journal of Advanced Joining Processes 2024;9:100194. https://doi.org/10.1016/j.jajp.2024.100194.
[17] Ferhat Ceritbinmez, Ali Günen, Ugur Gürol, Gürel Çam, A comparative study on drillability of Inconel 625 alloy fabricated by wire arc additive manufacturing, Journal of Manufacturing Processing, 89(3), 28, 150-169. https://doi.org/10.1016/j.jmapro.2023.01.072.
[18] Lippold JC. Welding metallurgy and weldability. In: Welding metallurgy and weldability. Wiley; 2015. https://doi.org/10.1002/9781118960332.
[19] Li S, Wei Q, Shi Y, Zhu Z, Zhang D. Microstructure characteristics of Inconel 625 Superalloy manufactured by selective laser melting. J Mater Sci Technol 2015;31(9):946–52. https://doi.org/10.1016/j.jmst.2014.09.020.
[20] Lass EA, Stoudt MR, Williams ME, Katz MB, Levine LE, Phan TQ, Gnaeupel-Herold TH, Ng DS. Formation of the Ni3Nb δ-phase in stress-relieved Inconel 625 produced via laser powder-bed fusion additive manufacturing. Metall Mater Trans A 2017;48:5547–58. https://doi.org/10.1007/s11661-17-4304-6.
[21] Chandler H. Heat treater's guide: practices and procedures for nonferrous alloys. ASM International; 1996.
[22] Radavich JF, Fort A. Effects of long time exposure in alloy 625 at 1200°F, 1400°F and 1600°F. Superalloys 1994;718:635–47. https://doi.org/10.7449/1994/Superalloys_1994_635_647.
[23] Shankar V, Bhanu Sankara Rao K, Mannan SL. Microstructure and mechanical properties of Inconel 625 superalloy. J Nucl Mater 2001;288(2–3):222–32. https://doi.org/10.1016/S0022-3115(00)00723-6.
[24] Mu Y, Wang C, Zhou W, Zhou L. Effect of Nb on δ phase precipitation and the tensile properties in cast alloy IN625. Metals 2018;8(2):86. https://doi.org/10.3390/met8020086.
[25] Betts Joseph, Glanvill Sarah, Shokrani Alborz. Impact of directionality and heat treatment on machining of additively manufactured Inconel 718. CIRP Ann - Manuf Technol 2024;73:69–77. https://doi.org/10.1016/j.cirp.2024.04.057.
[26] Sharma Himanshu, Singla Jonny, Singh Vikrant, Singh Jagtar, Kumar Hitesh, Bansal Anuj, Singla Anil Kumar, Goyal Deepak Kumar, Gupta Munish Kumar. Influence of post heat treatment on metallurgical, mechanical, and corrosion analysis of wire arc additive manufactured inconel 625. J Mater Res Technol 2023;27:5910–23. https://doi.org/10.1016/j.jmrt.2023.11.074.
[27] Karabulut Y, Tascioglu E, Kaynak Y. Heat treatment temperature-induced microstructure, microhardness and wear resistance of Inconel 718 produced by selective laser melting additive manufacturing. Optik 2019. https://doi.org/10.1016/j.ijleo.2019.163907.
[28] Gallmeyer Thomas G, Moorthy Senthamilaruvi, Kappes Branden B, Mills Michael J, Amin-Ahmadi Behnam, Stebner Aaron P. Knowledge of process-structure-property relationships to engineer better heat treatments for laser powder bed fusion additive manufactured Inconel 718. Addit Manuf 2020;31:100977. https://doi.org/10.1016/j.addma.2019.100977.
[29] Park SC, Banf HS, Seong WJ. Effect of material properties on angular distortion in wire arc additive manufacturing: experimental and computational analysis. Materials 2020;13:6. https://doi.org/10.3390/ma13061399.
[30] Montevecchi F, et al. Finite element mesh coarsening for effective distortion prediction in wire arc additive manufacturing. Addit Manuf 2017;18:24–33. https://doi.org/10.1016/j.addma.2017.10.010.
[31] Manurung Yupiter HP, Prajadhiana Keval P, Adenan Mohd Shahriman, Awiszus Birgit, Graf Marcel, Haelsig Andre. Analysis of material property models on WAAM distortion using nonlinear numerical computation and experimental verification with P-GMAW. Arch Civ Mech Eng 2021;21:32. https://doi.org/10.1007/s43452-021-00189-4.
[32] Zheng Yi, Li Chuanzong, Xie Jingren, Yu Zhiyuan, Wang Yajie, Chen Jieshi, Lu Hao, Yu Chun. Effects of thermal history of in-situ thermal management on as-built property heterogeneity of plasma arc additively manufactured Inconel 625. J Mater Res Technol 2023;25:2645–75. https://doi.org/10.1016/j.jmrt.2023.06.090.
[33] Pramod R, Mohan Kumar S, Rajesh Kannan A, Siva Shanmugam N, Tangestani Reza. Fabrication of gas metal arc welding based wire plus arc additive manufactured 347 stainless steel structure: behavioral analysis through experimentation and finite element method. Met Mater Int 2022. https://doi.org/10.1007/s12540-021-01026-2.
[34] Li Y, Feng Z, Hao L, Huang L, Xin C, Wang Y, et al. A review on functionally graded materials and structures via additive manufacturing: from multi-scale design to versatile functional properties. Adv Mater Technol 2020;5. https://doi.org/10.1002/admt.201900981.
[35] Ghanavati R, Naffakh-Moosavy H. Additive manufacturing of functionally graded metallic materials: a review of experimental and numerical studies. J Mater Res Technol 2021;13:1628–64. https://doi.org/10.1016/j.jmrt.2021.05.022.
[36] Schneck M, Horn M, Schmitt M, Seidel C, Schlick G, Reinhart G. Review on additive hybrid- and multi-material manufacturing of metals by powder bed fusion: state of technology and development potential. Prog in Addit Manuf 2021;6:881–94. https://doi.org/10.1007/s40964-021-00205-2.
[37] Rodrigues Tiago A, Farias Francisco Werley Cipriano, Zhang Kaiping, Shamsolhodaei A, Shen Jiajia, Zhou N, Schell Norbert, Capek Jan, Polatidis E, Santos Telmo G, Oliveira JP. Wire and arc additive manufacturing of 316L stainless steel/Inconel 625 functionally graded material: development and characterization. J Mater Res Technol 2022;21:237–51. https://doi.org/10.1016/j.jmrt.2022.08.169.
[38] Carroll BE, Otis RA, Borgonia JP, Suh JO, Dillon RP, Shapiro AA, et al. Functionally graded material of 304L stainless steel and inconel 625 fabricated by directed energy deposition: characterization and thermodynamic modeling. Acta Mater 2016;108:46–54. https://doi.org/10.1016/j.actamat.2016.02.019.
[39] Tanvir ANM, Ahsan Md RU, Ji Changwook, Hawkins Wayne, Bates Brian, Kim Duck Bong. Heat treatment effects on Inconel 625 components fabricated by wire + arc additive manufacturing (WAAM)—Part 1: microstructural characterization. Int J Adv Manuf Technol 2019;103:3785–98. https://doi.org/10.1007/s00170-019-03828-6.
[40] Tanvir ANM, Ahsan MDRU, Seo Gijeong, Kim Jae-duk, Ji Changwook, Bates Brian, Lee Yousub, Kim Duck Bong. Heat treatment effects on Inconel 625 components fabricated by wire + arc additively manufacturing (WAAM)—Part 2: mechanical

properties. Int J Adv Manuf Technol 2020;110:1709–21. https://doi.org/10.1007/s00170-020-05980-w.
[41] Mishra Rajnish, Imam Murshid, Chinthapenta Vishwanath, Mastanaiah P. Thermo-mechanical modelling of the wire arc based additively manufactured Inconel 625 superalloy. Mater Today Proc 2023. https://doi.org/10.1016/j.matpr.2023.08.142.
[42] Montevecchi F, Venturini G, Scippa A, Campatelli G. Finite element modelling of wire-arc-additive-manufacturing process. Proced CIRP 2016;55:109–14.
[43] Cambon C, Bendaoud I, Rouquette S, Soulié F. Influence of the first weld bead on strain and stress states in wire+arc additive manufacturing. In: 12th int. Semin. '"Numerical Anal. Weldability.'"; 2018. https://hal.archives-ouvertes.fr/hal-01954354.
[44] Mishra R, Pillai A, Imam M, Chinthapenta V, Vineesh KP. Experimental and numerical investigation of double pass overlapping beads by twin-wire welding additive manufacturing process. Trans Indian Inst Met 2022:1–17.
[45] Du Zhenglin, Sun Xianchong, Ng Fern Lan, Chew Youxiang, Tan Chaolin, Bi Guijun. Thermo-metallurgical simulation and performance evaluation of hybrid laser arc welding of chromium-molybdenum steel. Mater Des 2021;210:110029. https://doi.org/10.1016/j.matdes.2021.110029.
[46] Chaudhary A, Mishra R, Anwar Ali Anshari Md, Imam M, Chintapenta V. Experimental and numerical investigation of laser-FSW hybrid welding technique for high strength materials. Mater Today Proc 2022;65:3437–48. https://doi.org/10.1016/j.matpr.2022.05.579.
[47] Chen C, Yin J, Zhu H, Xiao Z, Zhang L, Zeng X. Effect of overlap rate and pattern on residual stress in selective laser melting. Int J Mach Tool Manufact 2019;145:103433. https://doi.org/10.1016/j.ijmachtools.2019.103433.
[48] Prabhu Avinash. Influence of phase transformations on the residual stress evolution and cracking tendency in CM247LC nickel-base superalloy, PhD diss. University of Tennessee; 2019. https://trace.tennessee.edu/utk_graddiss/5746.
[49] Koistinen DP, Marburger RE. A general equation prescribing the extent of the austenite-martensite transformation in pure iron-carbon alloys and plain carbon steels. Acta Metall 1959;7:59–60. https://doi.org/10.1016/0001-6160(59)90170-1.
[50] Johnson WA, Mehl RF. Kinetics of phase change. I general theory. J Chem Phys 1939;7:1103–12. https://doi.org/10.1063/1.1750380.
[51] Avrami M. J. Chem. Kinetics of phase change. I general theory. Phys 1939;7:1103–12. https://doi.org/10.1063/1.1750380.
[52] Leblond JB, Devaux J. A new kinetic model for anisothermal metallurgical transformations in steels including effect of austenite grain size. Acta Metall 1984;32(1):137–46. https://doi.org/10.1016/0001-6160(84)90211-6.
[53] D V, Durairaj R. 3D finite element simulation of temperature distribution, residual stress and distortion on 304 stainless steel plates using GTA welding. J Mech Sci Techol 2016;30:67–76. https://doi.org/10.1007/s12206-015-1208-5.
[54] Kumar TS, Atikukke N, Kannan R. Thermal cycling effects on the creep-fatigue interaction in type 316LN austenitic stainless steel weld joint. Int J Pres Ves Pip 2019;178:1040. https://doi.org/10.1016/j.ijpvp.2019.104009.
[55] Hu Z, Qin X, Shao T. Welding thermal simulation and metallurgical characteristics analysis in WAAM for 5crnimo hot forging die remanufacturing. Proc Eng 2017;207:2203–8. https://doi.org/10.1016/j.proeng.2017.10.98.
[56] Ding Donghong, Zhang Shimin, Lu Qinghua, Pan Zengxi, Li Huijun, Wang Kai. The well-distributed volumetric heat source model for numerical simulation of wire arc additive manufacturing process. Mater Today Commun 2021;27:102430. https://doi.org/10.1016/j.mtcomm.2021.102430.
[57] Hussein A, Hao L, Yan C, Everson R. Finite element simulation of the temperature and stress fields in single layers built without-support in selective laser melting. Mater Des 2013;52:638. https://doi.org/10.1016/j.matdes.2013.05.070.
[58] Zhao H, Zhang G, Yin Z, Wu L. A 3D dynamic analysis of thermal behavior during single-pass multi-layer weld-based rapid prototyping. J Mater Process Technol 2011;211:488. https://doi.org/10.1016/j.jmatprotec.2010.11.002.
[59] Bai X, Colegrove P, Ding J, Zhou X, Diao C, Bridgeman P, Honnige JR, Zhang H, Williams S. Numerical analysis of heat transfer and fluid flow in multilayer deposition of PAW-based wire and arc additive manufacturing. Int J Heat Mass Tran 2018;124:504–16. https://doi.org/10.1016/j.ijheatmasstransfer.2018.03.085.
[60] Chua Bih-Lii, Lee Ho-Jin, Ahn Dong-Gyu, Wang Yeqing. A Study on activation Algorithm of finite elements for three-dimensional transient heat transfer analysis of directed energy deposition process. Int J Precis Eng Manuf 2019;20:863–9. https://doi.org/10.1007/s12541-019-00118-9.
[61] Fang XY, Li HQ, WangM Li C, Guo YB. Characterization of texture and grain boundary character distributions of selective laser melted Inconel 625 alloy. Mater Char 2018;143:182–90. https://doi.org/10.1016/j.matchar.2018.02.008.
[62] MarcheseG LorussoM, Parizia S, Bassini E, Lee JW, Calignano F, Manfredi D, Terner M, Hong HU, Ugues D, LombardiM Biamino S. Influence of heat treatments on microstructure evolution and mechanical properties of Inconel 625 processed by laser powder bed fusion. Mater Sci Eng A 2018;729:64–75. https://doi.org/10.1016/j.msea.2018.05.044.
[63] Sun Jiamin, Hensel Jonas, Köhler Markus, Dilger Klaus. Residual stress in wire and arc additively manufactured aluminum components. J Manuf Process 2021;65:97–111. https://doi.org/10.1016/j.jmapro.2021.02.021.
[64] Ding J, Colegrove P, Mehnen J, Williams S, Wang F, Sequeira Almeida P. A computationally efficient finite element model of wire and arc additive manufacture. Int J Adv Manuf Technol 2014;70:227–36. https://doi.org/10.1007/s00170-013-5261-x.
[65] Köhler M, Fiebig S, Hensel J, Dilger K. Wire and arc additive manufacturing of aluminum components. Metals 2019;9:1–9. https://doi.org/10.3390/met9050608.
[66] Lin Zidong, Song Kaijie, Yu Xinghua. A review on wire and arc additive manufacturing of titanium alloy. J Manuf Process 2021;70:24–45. https://doi.org/10.1016/j.jmapro.2021.08.018.
[67] Pan Z, Ding D, Wu B, Cuiuri D, Li H, Norrish J. Arc welding processes for additive manufacturing: a review. Trans Intelligent Welding Manuf 2018:3–24. https://doi.org/10.1007/978-981-10-5355-9_1.
[68] Srivastava S, Garg RK, Sharma VS, Sachdeva A. Measurement and mitigation of residual stress in wire-arc additive manufacturing: a review of macro-scale continuum modelling approach. Arch Comput Methods Eng 2020:1–25. https://doi.org/10.1007/s11831-020-09511-4.
[69] Shen H, Lin J, Zhou Z, et al. Effect of induction heat treatment on residual stress distribution of components fabricated by wire arc additive manufacturing. J Manuf Process 2022;75:331–45. https://doi.org/10.1016/j.jmapro.2022.01.018.
[70] Bagheri Vanani Behrouz, , Mohammad Reza Mehraban Dehaqani, Abbasi Mahmoud, Sadeqi Bajestani Mahdi, Mohammadkhah Melika, Klinge Sandra. Effects of PWHT on the microstructure, corrosion, tribology, and mechanical properties of mild steel welds under different joining positions: experimental and Numerical Study. Int J Manag Res Technol 2025;38:752–67. https://doi.org/10.1016/j.jmrt.2025.07.253.
[71] Ali Tahaei, Abbasi Mahmoud, Vanani Behrouz Bagheri, Zanotto Federica, Perez Argelia Fabiola Miranda. The role of nitrogen gas and PWHT on pitting corrosion behavior of duplex stainless-steel joint made by GTAW. Metallogr Microstruct Anal 2024;13:624–39. https://doi.org/10.1007/s13632-024-01105-x.
[72] Blakey-Milner B, Gradl P, Snedden G, Brooks M, Pitot J, Lopez E, et al. Metal additive manufacturing in aerospace: a review. Mater Des 2021;209:110008. https://doi.org/10.1016/j.matdes.2021.110008.
[73] Montevecchi F, Venturini G, Grossi N, Scippa A, Campatelli G. Idle time selection for wire-arc additive manufacturing: a finite element-based technique. Addit Manuf 2018;21:479–86. https://doi.org/10.1016/j.addma.2018.01.007.
[74] Ding D, Pan Z, Cuiuri D, Li H. Wire-feed additive manufacturing of metal components: technologies, developments and future interests. Int J Adv Manuf Technol 2015;81:465–81. https://doi.org/10.1007/s00170-015-7077-3.
[75] Bodner SC, Hlushko K, van de Vorst LTG, Meindlhumer M, Todt J, Nielsen MA, Hooijmans JW, Saurwalt JJ, Mirzaei S, Keckes J. Graded inconel-stainless steel multi-material structure by inter- and intralayer variation of metal alloys. J Mater Res Technol 2022;21:4846–59. https://doi.org/10.1016/j.jmrt.2022.11.064.
[76] Gamon A, Arrieta E, Gradl PR, Katsarelis C, Murr LE, Wicker RB, et al. Microstructure and hardness comparison of as-built inconel 625 alloy following various additive manufacturing processes. Results Mater 2021;12:100239. https://doi.org/10.1016/j.rinma.2021.100239.
[77] Li K, Chen W, Gong N, et al. A critical review on wire-arc directed energy deposition of high-performance steels. J Mater Res Technol 2023;24:9369–412. https://doi.org/10.1016/j.jmrt.2023.05.163.
[78] Megahed M, Mindt HW, N'Dri N, Duan H, Desmaison O. Metal additive-manufacturing process and residual stress modeling. Integrating Materials and Manufacturing Innovation 2016;5. https://doi.org/10.1186/s40192-016-0047-2.
[79] Abusalma H, Eisazadeh H, Hejripour F, et al. Parametric study of residual stress formation in wire and arc additive manufacturing. J Manuf Process 2022;75:863–76. https://doi.org/10.1016/j.jmapro.2022.01.043.